RESEARCH ARTICLE

Hierarchical platinum–iridium neural electrodes structured by femtosecond laser for superwicking interface and superior charge storage capacity

Linze Li[1] · Changqing Jiang[1] · Luming Li[1,2,3,4]

Abstract
The interfacial performance of implanted neural electrodes is crucial for stimulation safety and the recording quality of neuronal activity. This paper proposes a novel surface architecture and optimization strategy for the platinum–iridium (Pt–Ir) electrode to optimize electrochemical performance and wettability. A series of surface micro/nano structures were fabricated on Pt–Ir electrodes with different combinations of four adjustable laser-processing parameters. Subsequently, the electrodes were characterized by scanning electron microscopy, energy-dispersive X-ray spectroscopy, cyclic voltammetry, electrochemical impedance spectroscopy, and wetting behavior. The results show that electrode performance strongly depends on the surface morphology. Increasing scanning overlap along with moderate pulse energy and the right number of pulses leads to enriched surface micro/nano structures and improved electrode performance. It raises the maximum charge storage capacity to 128.2 mC/cm^2 and the interface capacitance of electrodes to 3.0×10^4 µF/cm^2 for the geometric area, compared with 4.6 mC/cm^2 and 443.1 µF/cm^2, respectively, for the smooth Pt–Ir electrode. The corresponding optimal results for the optically measured area are 111.8 mC/cm^2 and 2.6×10^4 µF/cm^2, which indicate the contribution of finer structures to the ablation profile. The hierarchical structures formed by the femtosecond laser dramatically enhanced the wettability of the electrode interface, giving it superwicking properties. A wicking speed of approximately 80 mm/s was reached. Our optimization strategy, leading to superior performance of the superwicking Pt–Ir interface, is promising for use in new neural electrodes.

Keywords Charge storage capacity · Femtosecond laser · Hierarchical structures · Neural electrodes · Superwicking

Article highlights

- A new surface architecture is proposed to greatly improve the electrochemical performance of Pt–Ir electrodes.
- The electrode surface with hierarchical structures exhibits superwicking behavior with the electrolyte (water).
- The processing parameters were optimized to produce enriched surface micro/nano structures and enhance electrode performance.

Introduction

Implanted electrodes used for neural stimulation and/or recording are essential components in neuromodulation devices and brain-computer interfaces, which are burgeoning and being successfully applied in disease treatments and physical rehabilitation [1]. For safe stimulation in these

✉ Changqing Jiang
jiangcq13@tsinghua.edu.cn

✉ Luming Li
lilm@tsinghua.edu.cn

1 National Engineering Laboratory for Neuromodulation, School of Aerospace Engineering, Tsinghua University, Beijing 100084, China

2 Precision Medicine and Healthcare Research Center, Tsinghua-Berkeley Shenzhen Institute, Tsinghua University, Shenzhen 518071, China

3 IDG/McGovern Institute for Brain Research at Tsinghua University, Beijing 100084, China

4 Institute of Epilepsy, Beijing Institute for Brain Disorders, Beijing 100093, China

applications, the electrode interface must allow the injection of enough charge while avoiding irreversible reduction and oxidation reactions [2]. Platinum or platinum–iridium (Pt–Ir) alloys are widely used for neural stimulation electrodes in active implantable medical devices (AIMD) such as deep brain stimulators (DBS), cochlear implants, and spinal cord stimulators, given their excellent biocompatibility and corrosion resistance [3]. However, their low charge-injection capacity limits further application to meet the increasing demand of sophisticated stimulation strategies requiring a smaller geometry [4]. Moreover, an electrode with small geometrical size is usually accompanied by high impedance, which affects not only stimulation efficiency but also recording quality [1].

Various approaches have been reported which optimize the electrode charge transfer properties and electrochemical impedance of Pt–Ir electrodes, typically involving additive coatings or surface modification. Electrode coatings such as iridium oxide [5], carbon nanotubes [6], or conductive polymers [7, 8] can significantly improve the charge injection capacity of the electrodes, by one to two orders of magnitude, with greatly reduced electrode impedance. Nevertheless, the chronic instabilities in an implant environment are still challenges to be overcome [9]. Surface modification provides an alternative approach, which is generally performed by roughening the Pt or Pt–Ir electrode surface. It has been reported that plasma etching [10] and electrochemical roughening [11] can produce significant enhancement in the surface area; however, the first requires a precise mask of the electrode patterns and the second some harmful chemical reagents.

Laser processing is another surface-modification method to produce various micro/nano structures by adjusting the processing parameters [12, 13]. The processes, such as resolidification after ablation and redeposition of nanoparticles, have been explained in detail previously to elucidate their formation mechanisms [14]. Green et al. [15] found that shortening laser pulse durations from nanoseconds to picoseconds reduced the heat-affected zone, leading to a larger active surface and no significant chemical changes that could block the electrode interface. Nevertheless, to date, charge transfer performance after laser processing has only been increased around two to five times, which is less than the increase from other techniques [15–18]. With a shorter pulse duration, the femtosecond laser technique is expected to provide abundant hierarchical structures on micro- and nano-scales, with further increased surface area.

Moreover, the creation of hierarchical structures by ultrafast laser direct writing has been a novel approach to producing a wicking surface, which might facilitate quick and thorough wetting of the electrode surface by the electrolyte [19]. It also may help prevent the problem of electrode dissolution during electrical stimulation, which is induced by a concentrated electric field formed by air trapped on the surfaces [15]. Vorobyev and Guo [20] reported that platinum structured by high-intensity femtosecond laser showed wicking behavior along the parallel grooves on the surface with methanol, due to the Marangoni effect on the volatile liquid. However, for a low-volatility liquid—water—which was the main substance surrounding the neural electrode, it exhibited repelling behavior. Preparation of Pt–Ir electrodes with better wettability for water and improved electrochemical performance is of great interest.

In this study, we systematically investigated the ablation characteristics and laser-induced surface structures on Pt–Ir electrodes by adjusting four processing parameters of the femtosecond laser: pulse energy, repetition rate, scanning speed, and scanning overlap. We characterized the evolutions of micro/nano structures, electrochemical performance, and wettability with various processing parameters. Through these investigations, we were able to determine an optimization strategy for the processing parameters, to generate superwicking Pt–Ir with superior electrochemical performance and great potential for novel implanted neural electrodes.

Materials and methods

Materials

A bare cylindrical Pt–Ir alloy tube with an outer diameter $D = 1.27$ mm and thickness $t = 100$ μm was used, as shown in Fig. 1 (90% Pt and 10% Ir, purchased from Johnson Matthey,
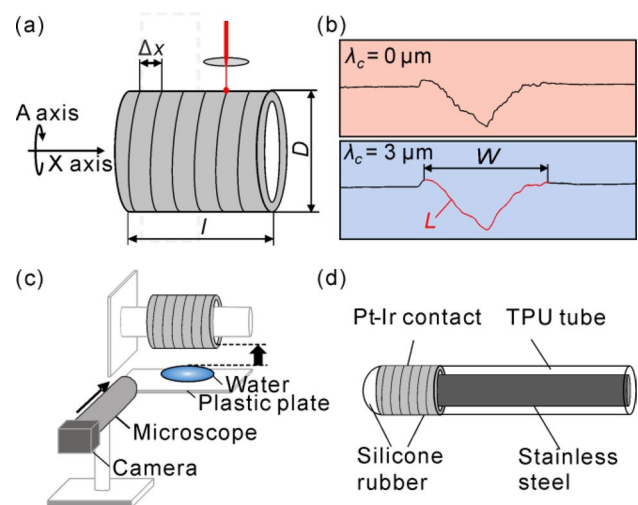

Fig. 1 Laser processing and characterization methods. **a** Schematic diagram of femtosecond laser processing on Pt–Ir tube. **b** Contour line of microgroove before and after filtering. **c** Wicking behavior characterization method. **d** Illustration of electrode structure

Inc., USA). The raw tube was cleaned with ethanol before laser treatment.

Laser irradiation

A Yb: KGW femtosecond laser system (StarCut 2 + 2, Rofin, Germany) was used to irradiate the as-prepared samples. The laser pulse width was 300 fs and the center wavelength was 1030 nm. The Pt–Ir tube was clamped with a three-jaw chuck of the machine tool motion system. By controlling the translation axis X and rotation axis A, helix line scanning could be performed on the tube surface, with a spacing of Δx in the atmospheric environment, as shown in Fig. 1a.

We divided the laser-processing experiments into two parts. First, the effective radius of the laser beam and the ablation characteristics of Pt–Ir were evaluated through one-pitch helix machining within a power range of $P = 0.5$–4 W, with an interval of 0.5 W at the repetition rates $f = 25$, 50, 100, 500 kHz, and a scanning speed v of 10 mm/s. One microgroove was cut under each set of conditions, resulting in a total of 32 microgrooves. Second, with all combinations of pulse energy E, scanning speed v, repetition rate f, and scanning overlap φ_{line}, we fabricated a series of micro/nano structures on the surfaces to evaluate the electrode performance (see Table 1). In total, 73 electrodes were prepared, including a smooth control. Notably, the interval and overlapped line scanning could be distinguished according to whether the scanning spacing Δx was longer or shorter than the ablation width W under the same laser parameters. For $\varphi_{line} = 0$, interval scanning was conducted with a constant Δx of 100 μm. For $\varphi_{line} > 0$ (overlap scanning), Δx was calculated as in Eq. (1), based on the ablation width W from interval scanning [21].

$$\Delta x = \left(1 - \varphi_{line}\right) \times W. \tag{1}$$

In addition, the number of pulses N could be calculated from scanning speed v and repetition rate f, as in Eq. (2) [22]:

$$N = \frac{2\omega_0 f}{v}, \tag{2}$$

where, ω_0 is the Gaussian beam radius at which the intensity drops to $1/e^2$ of its axial. Note that during the scanning

Table 1 Laser irradiation parameters for evaluation of electrode performance

Factor	E	f	v	$N = 2\omega_0 f/v$	φ_{line}
Unit	μJ	kHz	mm/s	–	%
Levels	5, 7.5, 10	100, 500	5, 10	514, 1028, 2570, 5140	0, 13, 30, 48, 65, 83

process, the laser spot is always moving, so the irradiation energy of each pulse is not uniform in any one spot. Thus, Eq. (2) is an approximate expression.

Surface geometry characterization

We obtained the laser three-dimensional (3D) topographic maps of all processed surfaces with a 3D laser scanning microscope (VK-X250K, Keyence, Japan) at a magnification of 50×. We also obtained the contour lines of the cross-sectional perpendicular to the line-scanning direction and filtered them with a cutoff wavelength λ_c of 3 μm for a uniform scale, as shown in Fig. 1b. Then, we measured the ablation width W, depth H, and cross-sectional profile length L. For each combination of parameters, we took three optical measurements at randomly selected locations, and calculated the average values and standard deviation. The ratio between the optically measured surface area of the laser-processed region and its nominal geometric area is defined as surface index (SI), namely $SI = L/W$.

Mathematical model for surface geometry

The pulse energy E of a Gaussian beam can be obtained as in Eq. (3):

$$E = \frac{\pi}{2}\omega_0^2 F_0, \tag{3}$$

where F_0 is the peak fluence at the center of the beam spot.

Due to the Gaussian energy distribution of a femtosecond laser beam, there is a relationship between quadratic ablation width W^2 and pulse energy E [23], as in Eq. (4):

$$W^2 = 2\omega_0^2 \ln\left(\frac{E}{E_{th}}\right), \tag{4}$$

where E_{th} is the ablation threshold.

Further, the ablation depth H is correlated with ablation rate ΔH and number of pulses N, as in Eq. (5):

$$H = \Delta H \times N. \tag{5}$$

Therefore, ΔH is derived from Eq. (6):

$$\Delta H = H/N. \tag{6}$$

Following from the principle of femtosecond laser processing of metal, the ablation rate ΔH could be divided logarithmically into two regimes as shown in Eqs. (7) and (8), depending on the laser pulse energy [24]; one dominated by the optical penetration and the other by the electron heat conduction.

$$\Delta H = \delta \ln \left(\frac{E}{E_{\text{th}}^{\delta}} \right) \tag{7}$$

and

$$\Delta H = l \ln \left(\frac{E}{E_{\text{th}}^{l}} \right), \tag{8}$$

where E_{th}^{δ} and E_{th}^{l} are the corresponding ablation thresholds in each regime. δ and l are the optical penetration depth and energy penetration depth of pulse energy.

For samples from the first part of the laser irradiation experiment, the quadratic ablation width W^2 and ablation rate ΔH scale linearly with logarithmic pulse energy $\ln E$, as in Eqs. (4), (7), and (8). Therefore, one can obtain ω_0 and the ablation performance of Pt–Ir. In addition, assuming the ablation profile is V-shaped, the relationships between SI and H/W could be given according to the Pythagorean theorem as in Eq. (9):

$$SI = L/W = \sqrt{1 + 4(H/W)^2}. \tag{9}$$

Electrode fabrication

For samples from the second part of the laser irradiation experiment, the Pt–Ir tube processed with various parameters was cut into lengths of $l = 1.5$ mm for electrode contacts. The inner side of each contact was electrically connected to stainless steel bars with a diameter of 0.8 mm by conductive glue (529, Ausbond, China); and the steel bars were covered with a thermoplastic polyurethane (TPU) tube (PC-3555D, Lubrizol, USA), as shown in Fig. 1d. Both ends of the contacts were sealed with silicone rubber (K705, Kafuter, China). To avoid contamination with air pollutants that could affect the wettability of surfaces, all electrodes were kept in water before testing.

Surface morphology and chemical composition characterization

We analyzed the micro/nano structures of electrodes with a field-emission scanning electron microscope (FESEM) operating at 5 kV (Merlin, Zeiss, Germany). The surface element composition on the electrode contact was analyzed by energy-dispersive X-ray spectroscopy (EDS) using the same equipment.

Cyclic voltammetry

We performed cyclic voltammetry (CV) on the electrodes using an electrochemical workstation (Reference 600 Plus, Gamry, USA). A three-electrode system was used, in which the working electrodes were laser processing electrodes, the counter electrode was a titanium plate (20 mm × 30 mm × 0.3 mm), and the reference electrode was a KCl-saturated Ag/AgCl electrode (Type 218, Leici, China). The electrolyte solution was $1 \times$ PBS phosphate buffer solution (0.01 M, Solarbio, China). The scan started from the open circuit potential at a rate of 50 mV/s between -0.7 V and 0.7 V versus the reference electrode. For the untreated smooth electrode and the electrodes processed with overlap line scanning, the charge storage capacity (CSC) was obtained by integrating the cathode current density over time. For electrodes processed with interval line scanning, we calculated the CSC of the ablation zone by excluding the contribution of the smooth zone. To differentiate, CSC_{geo} is defined as the CSC by dividing the nominal geometric area, and CSC_{op} is defined by dividing the area measured by the optical profilometry (OP). The relationship is $CSC_{\text{geo}} = CSC_{\text{op}} \times SI$. Therefore, CSC_{op} denotes the contribution of nanostructures by excluding the influence of the optical profile (referred to as microstructure in this paper). CSC_{op} enlargement compared with the smooth control could be used to estimate the roughness r of the optical profile.

Electrochemical impedance spectroscopy

Electrochemical impedance spectroscopy (EIS) was measured after CV. The amplitude of the sinusoidal voltage excitation was 10 mV, and the test frequency ranged from 0.1 Hz to 100 kHz. We used Gamry Echem Analyst software (Version 7.06, Gamry, USA) to fit the circuit models according to the EIS curve.

Wicking behavior characterization

The wicking behavior was characterized as shown in Fig. 1c. A 0.3 μL water droplet was placed onto a plastic plate using a pipette and raised upward to the horizontally placed Pt–Ir contact until it reached its lower boundary. The wicking process was recorded by a camera with a microscope at 40 frames per second until no more movement was detected. The wetting state of the contact was analyzed frame by frame.

Results

Ablation characteristics evaluation of Pt–Ir

Figure 2 shows the results of optical geometry characterization of samples processed under different ablation parameters. The quadratic ablation width W^2 linearly increases with $\ln E$, and no obvious correlation with the repetition rate f was found (Fig. 2a). The slope of the fitting line indicates that
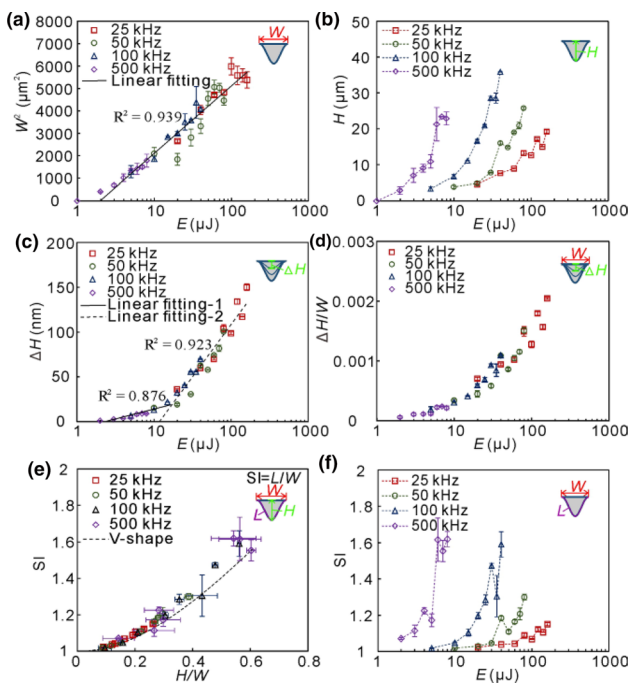
Fig. 2 Ablation performance of Pt–Ir. Effects of pulse energy E on **a** ablation width W^2, **b** depth H, **c** ablation rate ΔH, **d** ratio of $\Delta H/W$, and **f** SI. **e** Relationship between SI and H/W

the effective beam radius $\omega_0 = 25.7\ \mu m$, and the horizontal intercept represents the ablation threshold $E_{th} = 1.98\ \mu J$.

It is evident from Fig. 2b that the ablation depth H increased with $\ln E$ at the respective repetition rate f, and the magnitudes of curves increases with f. However, Fig. 2c shows that the ablation rate ΔH linearly increased with $\ln E$ in both regimes, and the rates did not show an obvious correlation with f. Therefore, the varied magnitudes of curves with f in Fig. 2b were mainly due to the different number of pulses N received at each position, as in Eqs. (2) and (5). The ΔH of both regimes could be fitted with $\ln E$, and were dominated by either optical penetration or electron heat conduction. The fitting slopes were 9.92 and 50.7 nm, and the pulse energy thresholds were 2.47 and 11.8 μJ, respectively, for the first and second regimes. The intersection of two fitting lines was 17.3 μJ. In addition, the point at 1 μJ, 500 kHz showed no observable ablation, due to its pulse energy being lower than the ablation threshold. The W and H of this point were 0, as shown in Figs. 2a and 2b, and it was excluded from the analysis in Figs. 2c–2f.

Further, the $\Delta H/W$ ratio also showed a monotonically increasing relation with $\ln E$, as seen in Fig. 2d. Thus, by increasing the number of pulses N and the pulse energy E, a large H/W could be obtained. In addition, SI increased with H/W (see Fig. 2e), which was slightly higher than the curve of the V-shape. Therefore, it could be inferred that the SI exhibited a similar relationship with processing parameters

as H/W, which also increased with N and E, as shown in Fig. 2f. This provides an approach to enlarge the optical surface area. Nevertheless, the SI amplitude was consistently below 1.8.

Effect of laser-processing parameters on micro/nanostructures and surface chemistry

With the changes in laser-processing parameters, we were able to classify six representative surface structures, as shown in the six rows in Fig. 3. We chose to call them Smooth, Interval 1, Interval 2, Overlap 1, Overlap 2, and Overlap 3. The first type is the Pt–Ir tube without laser irradiation, which was relatively smooth without obvious micro/nano structures. The second and third types were processed by interval line scanning at the same spacing of 100 μm, and displayed microgrooves in 400 × SEM images. With a higher repetition rate and pulse energy and lower scanning speed, the micro-protrusions became richer and were covered by denser nanoparticles, as shown in the 5k × and 50k × SEM images. Thus, the surface structures shifted from Interval 1 to Interval 2. The 3D laser topographical map and longitudinal profiles of microgrooves also change from being smooth to rather rough due to the denser micro/nano structures. Notably, there were similar nanoparticles between microgrooves in Interval 2, as shown in the insets; however, no micro-protrusion was observed. With the same processing parameters as Interval 2 and decreased scanning spacing to make the microgrooves overlap, the microstructures shifted from the parallel wavy microgrooves in Overlap 1 ($\varphi_{line} = 30\%$) to rather flat fern-like structures in Overlap 2 ($\varphi_{line} = 83\%$). The turning point occurred between φ_{line} values of 48% and 65% in overlap scanning, with all combinations of processing parameters. Although the microgrooves gradually disappeared, enriched micro-protrusions with abundant nanoparticles could be seen, which suggests a large surface area. At $\varphi_{line} = 83\%$, with the other processing parameters identical to those for Interval 1, the process also produced a rather flat but dense structure similar to Overlap 2, which is named Overlap 3. The periodic scanning traces for Overlap 3 remained observable both in the SEM images and the longitudinal profile, unlike those for Overlap 2.

The surface elemental compositions showed almost no change before and after femtosecond laser processing (Fig. S1 in the supplementary information).

Effect of laser-processing parameters on charge storage capacity

Based on the CV results, we obtained the cathodal charge storage capacity (CSC_c) for the optical profile of electrodes under different laser-processing parameters (Fig. 4a). As φ_{line} increased from 0 to 83%, CSC_{op} generally increased
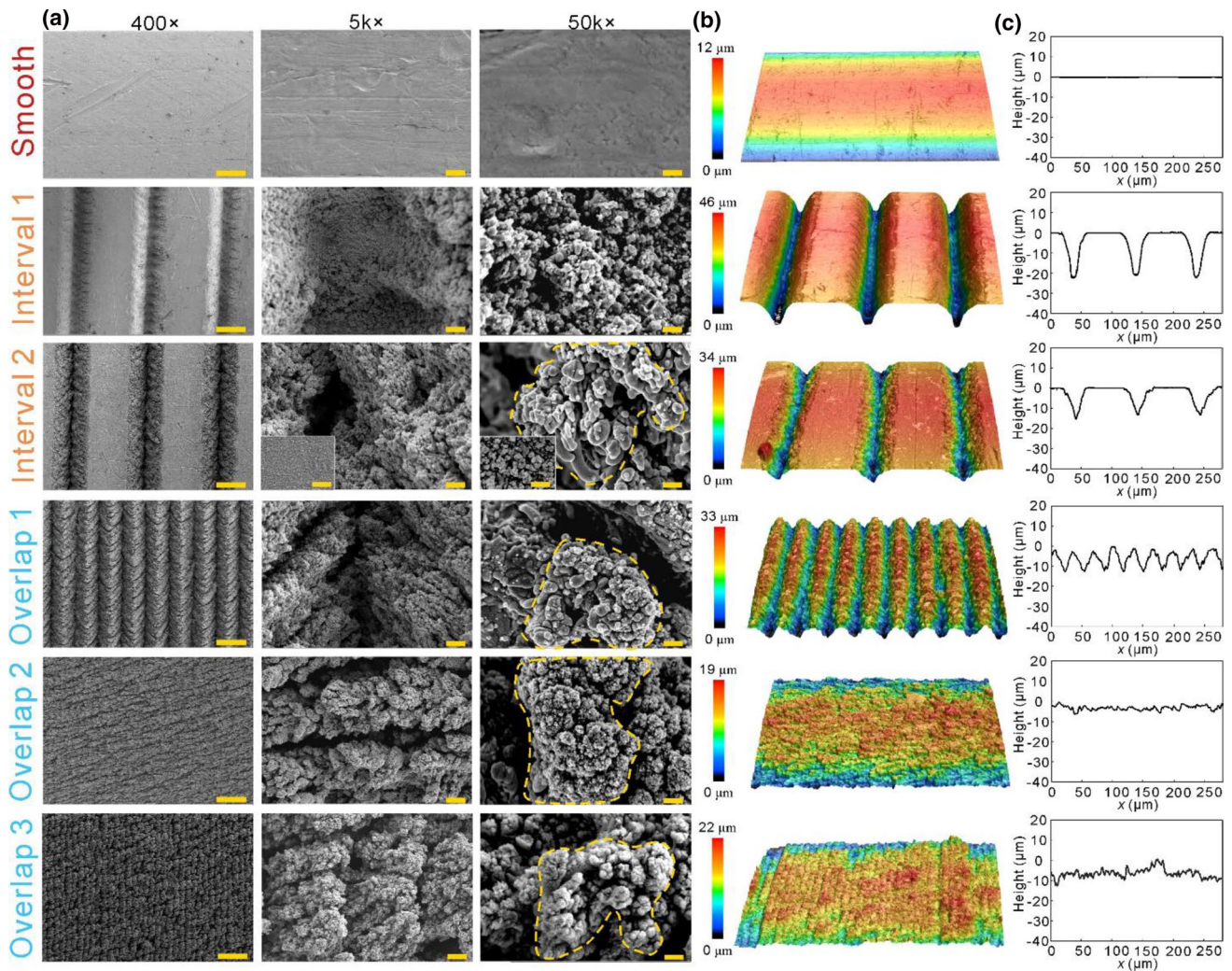
Fig. 3 Surface micro-/nanostructures. **a** SEM images of micro/nano structures. Scale bars are 40 μm, 2 μm, and 200 nm, respectively. Dotted lines circle the micro-protrusions. **b** 3D laser topographic map. **c** Longitudinal profiles on top of electrodes without filtering. The insets in interval 2 show the nanoparticle structure between microgrooves

with various combinations of E and N. Further, with constant φ_{line} values, both elevated E and elevated N tended to increase CSC_{op} when $\varphi_{line} = 0$ (interval scanning), as shown in Fig. 4b. However, a decreasing trend of CSC_{op} appeared with simultaneous increase in E and N in highly overlapped scanning when $\varphi_{line} = 83\%$. Both the maximum CSC_{op} and maximum CSC_{geo} occurred in Overlap 3, with values of 111.8 mC/cm^2 and 128.2 mC/cm^2; these were 24 and 28 times the values for the smooth control, which were both 4.6 mC/cm^2 for the optically measured and the nominal geometric areas with SI = 1.01. In Fig. 4c, we see that the corresponding SI at both $\varphi_{line} = 0$ and $\varphi_{line} = 83\%$ varied around 1–2, far smaller values than those produced by the CSC enlargements. Therefore, the nanostructures on the optical profile play an important role in improved electrode performance.

Effect of laser-processing parameters on impedance properties

Figure 5 shows the EIS results for six representative electrodes. The impedance magnitudes were significantly reduced after laser processing, especially for the electrodes scanned with overlap. Along with a reduction in magnitude, the phase was also shifted to lower frequencies, most likely as a result of increase in capacitive components. This indicates the formation of higher active surface area due to enriched nanostructures.

We used the equivalent circuit model, including a constant phase element (CPE), and the fitting results are shown as full lines in Fig. 5; they are in agreement with the experimental data points. The parameters are listed in
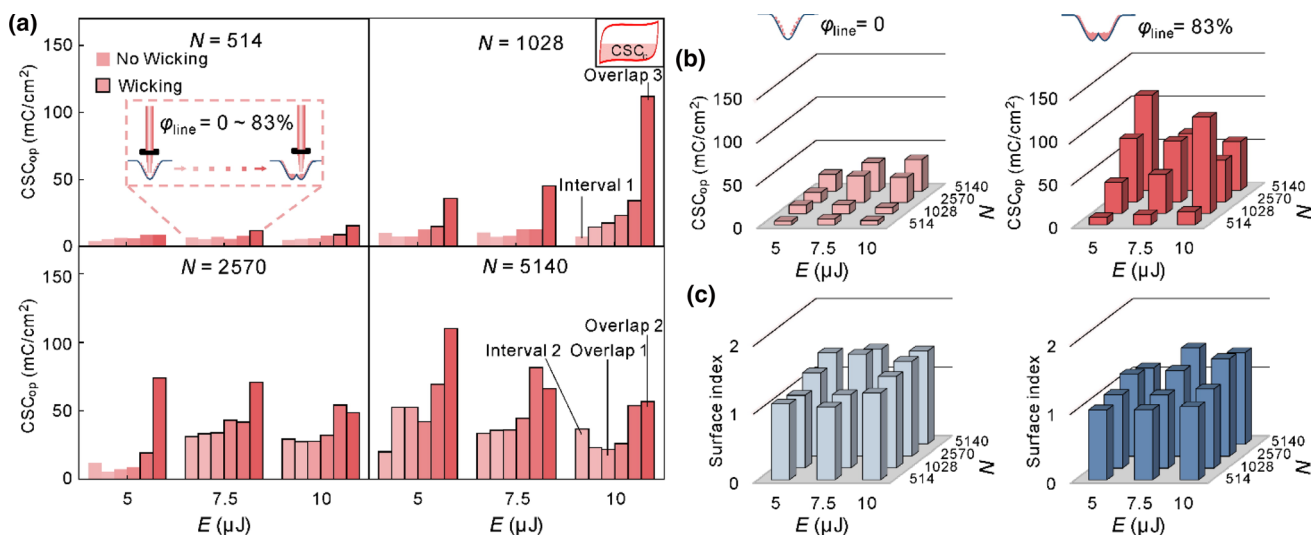
Fig. 4 **a** CSC_{op} under various combinations of E, N, and φ_{line}. Effects of E and N on **b** CSC_{op} and **c** optically measured surface index (SI) under $\varphi_{line} = 0$ and 83%
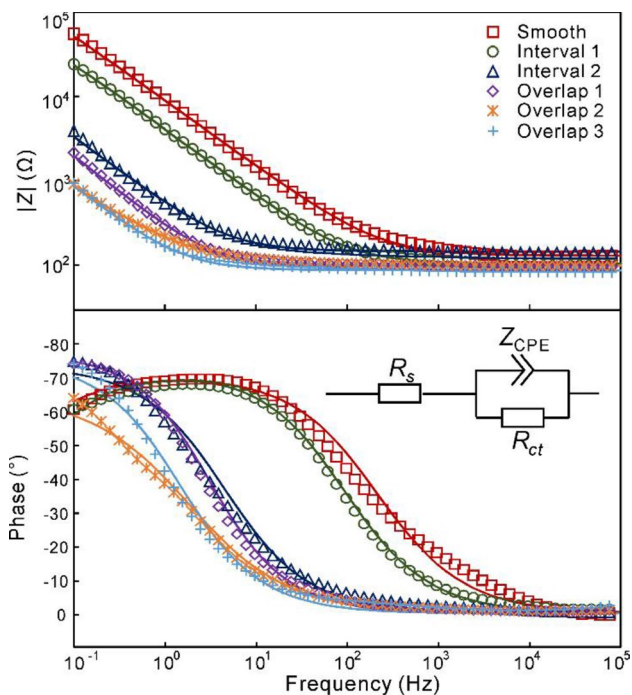
Fig. 5 Bode plot of electrochemical impedance of different types of electrodes

Table 2 Fitting results of different types of electrodes

Parameter	R_S	Y_0	α	R_{ct}
Unit	Ω	$\mu Fs^{\alpha-1}/cm^2$	$0 < \alpha < 1$	$M\Omega$
Smooth	124.2	443.1	0.79	0.35
Interval 1	96.7	988.8	0.81	0.093
Interval 2	139.2	7566.9	0.82	5900
Overlap 1	94.0	13 073.6	0.78	0.15
Overlap 2	94.6	29 949.8	0.72	3429
Overlap 3	74.1	30 200.7	0.84	3178

Effect of laser-processing parameters on wicking behaviors

The wicking behaviors of six representative electrodes are shown in Fig. 6 (see also the supplementary movies). For Smooth and Interval 1, only the lower part of the surface was in contact with the water drop, and no wicking behavior occurred. For both Interval 2 and Overlap 1, water spontaneously moved upward against gravity and reached the top of the center groove within 0.025 s, which translates to a transient wicking speed of about 80 mm/s. Overlap 1 was entirely wetted in 0.25 s. For Overlap 2 and Overlap 3, it was difficult to observe the wicking behavior in the photos; however, the water droplet was almost absorbed within 3 s, which also suggested a super-hydrophilic nature. In addition, we found that the wicking behavior occurred in all prepared electrodes when CSC_{op} exceeded a certain threshold (Figs. 4 and S2).

Table 2. One can see that the phase factor α is around 0.8, and the value of magnitude factor Y_0 keeps increasing, from 443.1 $\mu F/cm^2$ for the Smooth, to 2.6×10^4 $\mu F/cm^2$ and 3.0×10^4 $\mu F/cm^2$ for Overlap 3. These measurements were taken on the optically measured area and geometric area, and indicate increased interfacial capacitance.
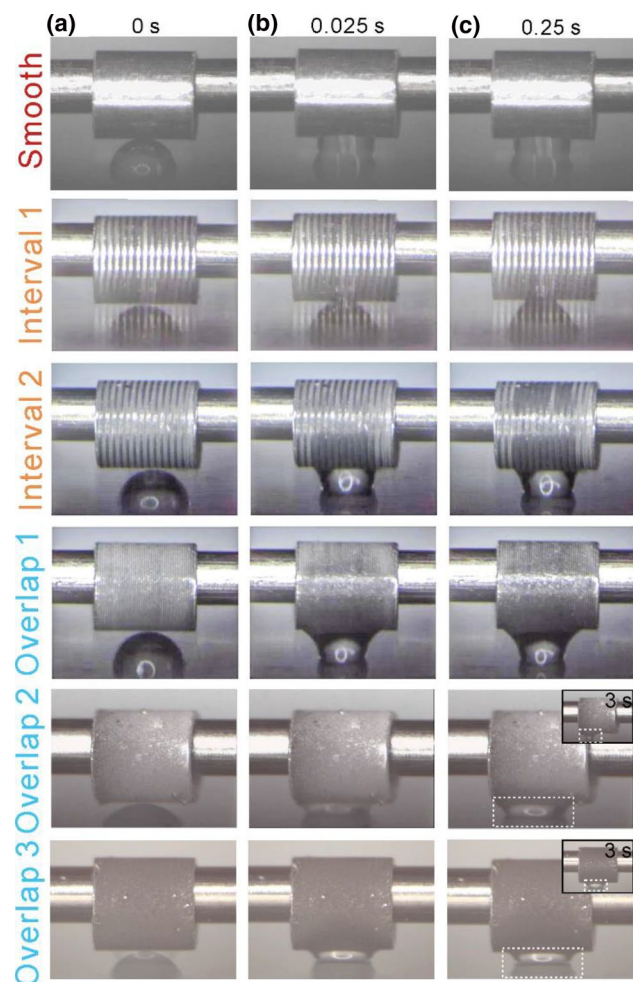
Fig. 6 Wicking behaviors of different types of electrodes. Video frames at **a** 0 s, **b** 0.025 s, and **c** 0.25 s. The dotted squares in Overlap 2 and Overlap 3 mark the droplets being absorbed during 0.25 to 3 s

Discussion

Electrochemical properties of implanted neural electrodes are critical for both stimulation and recording performance. In this study, we focused on improving the limited charge transfer performance of Pt–Ir for practical application. The Pt–Ir electrodes were processed by a femtosecond laser that produced a series of micro/nano structures on the surface. We demonstrated that the enriched hierarchical structures resulted in significant increase in CSC and reduction in electrochemical impedance. Moreover, superwicking behavior was observed at the electrode-solution interface, which takes advantage of the entire hidden surface area and opens up potential directions for future electrode design.

Femtosecond laser processing has been recognized as an efficient approach to create numerous surface structures with reduced heat-affected zones, through ultrashort pulses. Because of the unique threshold effect, when the pulse

energy is around the threshold value, a quasi-periodic structure with particles or ripples will be produced [12, 25]. In this study, the pulse energy was significantly higher than the ablation threshold, and the material was precisely ablated, as shown in Fig. 2. In a multi-pulse ablation, especially at a high repetition rate, the ablation threshold might decrease with an increasing number of pulses N; this is known as the incubation effect [26]. It may be attributed to the accumulation of laser-induced chemical and structural changes in the material or plastic deformation of the surface [27]. However, the results of both ablation width and ablation rate which are observable in Fig. 2 do not show an obvious correlation with the repetition rate. That is, there is no significant change in the ablation threshold. This agrees with findings on femtosecond laser processing of nickel, copper, titanium alloy, stainless steel 316L, and other metals with a repetition rate of 31–500 kHz [28]. In this case, the scanning speed and the repetition rate play important roles to the ablation contour by changing the number of pulses.

In addition to the precisely processed microgrooves, abundant smaller-scale micro/nano structures can be found, including micro-protrusions and nanoparticles, which are considered to be formed by different mechanisms. The nanoparticles appear both inside and outside the laser irradiation area and have similar sizes (Fig. 3); they are generally considered to be produced from the nucleation and redeposition of plasma plumes [29, 30]. For micro-protrusions, various formation mechanisms have been proposed for different materials [31–33]. The ablation surface topographies and formation process on Pt–Ir have not been thoroughly investigated before, but the result is very close to that in copper, which has been reported [21]. Ahmmed et al. [21] provided a perspective on the evolution of surface micro/nano structures produced by femtosecond laser based on the materials properties, without considering incubation effects. For the high-thermal-conductivity material platinum, as well as for copper, the rapid solidification of the molten phase along with the effect of surface capillary force could explain the formation of plentiful abnormally shaped protrusions [34, 35]. Intriguingly, for the overlap scanning with φ_{line} up to 65% with various combinations of processing parameters, the surfaces are completely covered by micro-protrusions and nanoparticles without obvious microgrooves, an effect which has also been found in copper. The formation mechanisms are worth exploring further in future work. The enhanced amount of the solidified molten phase and plasma plume deposition under high temperature might explain the formation of enriched micro-protrusions and nanoparticles.

The active surface area of Pt–Ir electrodes depends greatly on electrode surface morphology [15]. In this study, the fact that there is no significant change in chemical composition after laser processing promotes full utilization of the charge transfer interface. The contribution of microstructures

above 3 μm is limited, and the smaller-scale structures are supposed to play a more important role. This is in agreement with the SEM results, which indicate the presence of enriched micro-protrusions and nanoparticles. With regard to processing parameters, increased φ_{line} leads to denser structures due to decreased Δx [36, 37]. Therefore, higher CSC is obtained. Increasing both E and N leads to intense ablation with more micro-protrusions and nanoparticles in microgrooves, evident under interval scanning [36–38], and also increases CSC. However, under highly overlapped scanning, further increasing E and N simultaneously might result in too much stack, which blocks the already formed structures. An example of this is the complete disappearance of scanning traces in the SEM of Overlap 2 [37]. Therefore, it is clear that in this scenario, the CSC tends to decrease. Nevertheless, the maximum cathodal CSC of the wicking Pt–Ir electrode in this study reaches a comparable level of universal coating and carbon nanotube yarn under similar test conditions, as shown in Table 3. The information on these relationships between CSC and processing parameters could benefit future design of high-performance electrodes.

The electrodes with higher CSCs also show reduced impedance with increased capacitance. Usually, lower electrochemical impedance has the potential to enhance the stimulation safety and recording quality imparted by reduced power consumption. The larger capacitance after laser processing is thought to generate a larger volume of tissue activated for electrical stimulation [41]. Green et al. [15] suggest that the high capacitance after laser processing may come from not only the increased electrode surface area, but also the enhanced binding efficiency between ions and electrodes due to high surface energy. However, it was difficult to distinguish the two factors in this study, and this aspect is deserving of more research.

Table 3 Comparison between proposed design and reported works

No	Materials	Test conditions	CSC$_c$ (mC/cm^2)	Reference
1	Pt–Ir	$-0.7 \sim 0.7$ V, 50 mV/s	4.6	This work
2	Wicking Pt–Ir	$-0.7 \sim 0.7$ V, 50 mV/s	128.2	This work
3	Electrodeposited IrOx	$-0.6 \sim 0.6$ V, 50 mV/s	43	[5]
4	Sputtered IrOx	$-0.6 \sim 0.8$ V, 50 mV/s	194	[39]
5	Actived IrOx	$-0.6 \sim 0.8$ V, 50 mV/s	17	[40]
6	PEDOT	$-0.8 \sim 0.6$ V, 50 m V/s	75.6	[8]
7	CNT yarn	$-0.7 \sim 0.7$ V, 50 mV/s	98.6	[4]

The increased surface area not only improves electrochemical performance, but also induces superwicking behavior on the surface. Based on the interface energy balance, Rye et al. [42] proposed that the V-shaped groove requires an incline angle β larger than the contact angle of the substrate material to achieve wicking behavior. In this study, as pictured in Fig. 2e, the microgroove can be approximately regarded as a V-shape. With different processing parameters, the aspect ratio of the microgrooves on the Pt–Ir surface is always below 1.8, corresponding to $\beta = 56°$, which is smaller than the contact angle of water on the smooth Pt–Ir surface (about 78°). However, according to the Wenzel model, the contact angle of a rough surface can be described by Eq. (10) [18]:

$$\cos(\theta^*) = r\cos\theta, \qquad (10)$$

where θ and θ^* are the intrinsic and apparent contact angle and r is the roughness factor defined by the ratio of actual surface area to the geometrically projected area on the surface plane. That is, r can decrease the apparent contact angle θ^* due to $\theta < 90°$, which means a more hydrophilic surface [19]. Thus, a critical value of r, named r_{th}, is expected to induce wicking behavior. In this work, we were able to estimate r on the optical profile by the amount of CSC$_{op}$ enlargement compared to the smooth control. Results show that when r approaches or exceeds r_{th}, the surface begins to wick, which does not happen otherwise (Fig. S2). Therefore, the role of nanostructures cannot be ignored in the wicking behavior, in addition to microgrooves [43, 44]. The Pt–Ir neural electrodes with wicking behavior are expected to prevent the problem of electrode dissolution caused by air bubbles during electrical stimulation [15]. The quick and thorough wetting of the electrodes by water also promotes utilization of the hidden surface area. Notably, the high-free-energy surfaces tend to adsorb pollutants from the air, leading to hydrophobic surfaces and air trapping. Therefore, care needs to be taken regarding the storage environment of the electrodes.

Changes in surface topology and wettability can affect protein adsorption, cell adhesion, and inflammatory response, and the long-term performance of these electrodes in the implant environment requires more investigation [45, 46]. According to ISO 10,993–22:2017, in contrast to free nanoparticles and the release of nano-objects with potential internal exposure, medical devices containing nanostructured surfaces should be evaluated for potential cellular or tissue effects due to direct interaction [47, 48]. For neural electrodes, nanostructured surfaces have aroused increasing interest because of their potential to control cell adhesion [12, 45]. Several studies suggest that the nanostructures might provide intrinsic cues for neural adhesion in preference to astrocytes, which could improve

the physical coupling between neurons and electrodes, as well as facilitating stimulation efficiency and recording quality [25, 46, 49]. This is indicated by the increased surface coverage ratio of neurons compared with astrocytes through in vitro cell culture on the nanostructured surface, in contrast to a flat surface [49]. In addition, recent studies have shown the promise of nanoscale-architecture for controlling protein adsorption and reducing glial scar and inflammatory markers [46]. Nevertheless, the responses depend on the cell characteristics, in addition to surface morphology such as the size and distribution of nanoparticles [25, 45]. The topography with optimal in vivo biocompatibility for Pt–Ir electrodes merits more exploration before further application.

Conclusions

We propose a superwicking Pt–Ir neural electrode modified by femtosecond laser processing, which offers highly improved electrical performance and wettability. Increased scanning overlap with moderate pulse energy and number of pulses can enhance the charge storage capacity of the electrode, along with reduced electrochemical impedance and large interface capacitance, due to enriched surface micro/nano structures. The enriched micro-protrusions and nanoparticles play a more important role than the microgrooves. Electrodes with CSC_{op} enlargement above a certain threshold tend to exhibit wicking behavior with the aid of hierarchical structures. The water flow on the hierarchical Pt–Ir surface reaches speeds up to 80 mm/s, and thus the surface exhibits superwicking behavior. The unique performance achieved in situ on the commonly used Pt–Ir indicates a great opportunity for use in clinical neural electrodes.

Declarations

Conflict of interest The authors declare that they have no conflict of interest.

Ethical approval This study does not contain any studies with human or animal subjects performed by any of the authors.

References

1. Cogan SF (2008) Neural stimulation and recording electrodes. Annu Rev Biomed Eng 10:275–309. https://doi.org/10.1146/annurev.bioeng.10.061807.160518

2. Merrill DR, Bikson M, Jefferys JGR (2005) Electrical stimulation of excitable tissue: design of efficacious and safe protocols. J Neurosci Meth 141(2):171–198. https://doi.org/10.1016/j.jneumeth.2004.10.020

3. Cowley A, Woodward B (2011) A healthy future: platinum in medical applications. Platinum Metals Rev 55(2):98–107. https://doi.org/10.1595/147106711X566816

4. Jiang C, Li L, Hao H (2011) Carbon nanotube yarns for deep brain stimulation electrode. IEEE Trans Neur Syst Rehabil Eng 19(6):612–616. https://doi.org/10.1109/TNSRE.2011.2165733

5. Deku F, Joshi-Imre A, Mertiri A et al (2018) Electrodeposited iridium oxide on carbon fiber ultramicroelectrodes for neural recording and stimulation. J Electrochem Soc 165(9):D375–D380. https://doi.org/10.1149/2.0401809jes

6. Luo X, Weaver CL, Zhou DD et al (2011) Highly stable carbon nanotube doped poly(3,4-ethylenedioxythiophene) for chronic neural stimulation. Biomaterials 32(24):5551–5557. https://doi.org/10.1016/j.biomaterials.2011.04.051

7. Aqrawe Z, Wright B, Patel N et al (2019) The influence of macropores on PEDOT/PSS microelectrode coatings for neuronal recording and stimulation. Sens Actuat B Chem 281:549–560. https://doi.org/10.1016/j.snb.2018.10.099

8. Wilks S, Richardson-Burns SM, Hendricks JL et al (2009) Poly(3,4-ethylene dioxythiophene) (PEDOT) as a micro-neural interface material for electrostimulation. Front Neuroeng 2:7. https://doi.org/10.3389/neuro.16.007.2009

9. Aregueta-Robles UA, Woolley AJ, Poole-Warren LA et al (2014) Organic electrode coatings for next-generation neural interfaces. Front Neuroeng 7:1–18. https://doi.org/10.3389/fneng.2014.00015

10. Chung T, Wang JQ, Wang J et al (2015) Electrode modifications to lower electrode impedance and improve neural signal recording sensitivity. J Neur Eng 12(5):056018. https://doi.org/10.1088/1741-2560/12/5/056018

11. Ivanovskaya AN, Belle AM, Yorita AM et al (2018) Electrochemical roughening of thin-film platinum for neural probe arrays and biosensing applications. J Electrochem Soc 165(12):G3125–G3132. https://doi.org/10.1149/2.0171812jes

12. Vorobyev AY, Guo C (2009). Femtosecond laser surface structuring of biocompatible metals. In: Commercial and biomedical applications of ultrafast lasers IX, p 72030O. https://doi.org/10.1117/12.809593

13. Huo H, Shen M (2012) Platinum nanostructures formed by femtosecond laser irradiation in water. J Appl Phys 112(10):104314. https://doi.org/10.1063/1.4766407

14. Vorobyev AY, Guo C (2013) Direct femtosecond laser surface nano/microstructuring and its applications. Laser Photonics Rev 7(3):385–407. https://doi.org/10.1002/lpor.201200017

15. Green RA, Matteucci PB, Dodds CWD et al (2014) Laser patterning of platinum electrodes for safe neurostimulation. J Neur Eng 11(5):056017. https://doi.org/10.1088/1741-2560/11/5/056017

16. Schuettler M (2007) Electrochemical properties of platinum electrodes in vitro: comparison of six different surface qualities. In: 29th Annual International Conference of the IEEE Engineering

in Medicine and Biology Society, pp 186–189. https://doi.org/10.1109/IEMBS.2007.4352254

17. Mueller M, de la Oliva N, Del Valle J et al (2017) Rapid prototyping of flexible intrafascicular electrode arrays by picosecond laser structuring. J Neur Eng 14(6):066016. https://doi.org/10.1088/1741-2552/aa7eea

18. Sikder KU, Shivdasani MN, Fallon JB et al (2019) Electrically conducting diamond films grown on platinum foil for neural stimulation. J Neur Eng 16(6):066002. https://doi.org/10.1088/1741-2552/ab2e79

19. Vorobyev AY, Guo C (2015) Superwicking surfaces produced by femtosecond laser. In: Shulika O, Sukhoivanov I (eds) Advanced lasers, pp 101–115. https://doi.org/10.1007/978-94-017-9481-7_7

20. Vorobyev AY, Guo C (2009) Metal pumps liquid uphill. Appl Phys Lett 94(22):224102. https://doi.org/10.1063/1.3117237

21. Ahmmed KMT, Ling EJY, Servio P et al (2015) Introducing a new optimization tool for femtosecond laser-induced surface texturing on titanium, stainless steel, aluminum and copper. Opt Laser Eng 66:258–268. https://doi.org/10.1016/j.optlaseng.2014.09.017

22. Ahmmed KMT, Grambow C, Kietzig AM (2014) Fabrication of micro/nano structures on metals by femtosecond laser micromachining. Micromachines-Basel 5(4):1219–1253. https://doi.org/10.3390/mi5041219

23. Liu JM (1982) Simple technique for measurements of pulsed Gaussian-beam spot sizes. Opt Lett 7(5):196–198. https://doi.org/10.1364/ol.7.000196

24. Nolte S, Momma C, Jacobs H et al (1997) Ablation of metals by ultrashort laser pulses. J Opt Soc Am B 14(10):2716–2722. https://doi.org/10.1364/JOSAB.14.002716

25. Kelly A, Farid N, Krukiewicz K et al (2020) Laser-induced periodic surface structure enhances neuroelectrode charge transfer capabilities and modulates astrocyte function. Acs Biomater Sci Eng 6(3):1449–1461. https://doi.org/10.1021/acsbiomaterials.9b01321

26. Jee Y, Becker MF, Walser RM (1988) Laser-induced damage on single-crystal metal surfaces. J Opt Soc Am B 5(3):648. https://doi.org/10.1364/JOSAB.5.000648

27. Di Niso F, Gaudiuso C, Sibillano T et al (2014) Role of heat accumulation on the incubation effect in multi-shot laser ablation of stainless steel at high repetition rates. Opt Express 22(10):12200. https://doi.org/10.1364/OE.22.012200

28. Sedao X, Lenci M, Rudenko A et al (2019) Influence of pulse repetition rate on morphology and material removal rate of ultrafast laser ablated metallic surfaces. Opt Laser Eng 116:68–74. https://doi.org/10.1016/j.optlaseng.2018.12.009

29. Zhao X, Shin YC (2013) Femtosecond laser ablation of aluminum in vacuum and air at high laser intensity. Appl Surf Sci 283:94–99. https://doi.org/10.1016/j.apsusc.2013.06.037

30. Smausz T, Csizmadia T, Tápai C et al (2016) Study on the effect of ambient gas on nanostructure formation on metal surfaces during femtosecond laser ablation for fabrication of low-reflective surfaces. Appl Surf Sci 389:1113–1119. https://doi.org/10.1016/j.apsusc.2016.08.026

31. Ye S, Cao Q, Wang Q et al (2016) A highly efficient, stable, durable, and recyclable filter fabricated by femtosecond laser drilling of a titanium foil for oil-water separation. Sci Rep 6(1):37591. https://doi.org/10.1038/srep37591

32. Chiba T, Komura R, Mori A (2000) Formation of micropeak array on a silicon wafer. Jpn J Appl Phys 39(8R):4803–4810. https://doi.org/10.1143/JJAP.39.4803

33. Singh AK, Shinde D, More MA et al (2015) Enhanced field emission from nanosecond laser based surface micro-structured stainless steel. Appl Surf Sci 357:1313–1318. https://doi.org/10.1016/j.apsusc.2015.09.244

34. Tani S, Kobayashi Y (2018) Pulse-by-pulse depth profile measurement of femtosecond laser ablation on copper. Appl Phys A 124(3):265. https://doi.org/10.1007/s00339-018-1694-2

35. Biswas S, Karthikeyan A, Kietzig AM (2016) Effect of repetition rate on femtosecond laser-induced homogenous microstructures. Materials 9(12):1023. https://doi.org/10.3390/ma9121023

36. Long J, Pan L, Fan P et al (2016) Cassie-state stability of metallic superhydrophobic surfaces with various micro/nanostructures produced by a femtosecond laser. Langmuir 32(4):1065–1072. https://doi.org/10.1021/acs.langmuir.5b04329

37. Chen T, Wang W, Tao T et al (2020) Broad-band ultra-low-reflectivity multiscale micro–nano structures by the combination of femtosecond laser ablation and in situ deposition. ACS Appl Mater Interf 12(43):49265–49274. https://doi.org/10.1021/acsami.0c16894

38. Long J, Fan P, Gong D et al (2015) Superhydrophobic surfaces fabricated by femtosecond laser with tunable water adhesion: from lotus leaf to rose petal. ACS Appl Mater Interf 7(18):9858–9865. https://doi.org/10.1021/acsami.5b01870

39. Cogan SF, Ehrlich J, Plante TD et al (2009) Sputtered iridium oxide films for neural stimulation electrodes. J Biomed Mater Res B Appl Biomater 89(2):353–361. https://doi.org/10.1002/jbm.b.31223

40. Meyer RD, Nguyen TH, Twardoch UM, et al (1999). Electrodeposition of iridium oxide charge injection electrodes. In: IEEE Engineering in Medicine and Biology 21st Annual Conference and the 1999 Annual Fall Meeting of the Biomedical Engineering Society, pp 381–382. https://doi.org/10.1109/IEMBS.1999.802459

41. Butson CR, McIntyre CC (2005) Tissue and electrode capacitance reduce neural activation volumes during deep brain stimulation. Clin Neurophysiol 116(10):2490–2500. https://doi.org/10.1016/j.clinph.2005.06.023

42. Rye RR, Mann JA, Yost FG (1996) The flow of liquids in surface grooves. Langmuir 12:555–565. https://doi.org/10.1021/la9500989

43. Li X, Yuan G, Yu W et al (2020) A self-driven microfluidic surface-enhanced Raman scattering device for Hg^{2+} detection fabricated by femtosecond laser. Lab Chip 20(2):414–423. https://doi.org/10.1039/c9lc00883g

44. Aguilar-Morales AI, Alamri S, Voisiat B et al (2019) The role of the surface nano-roughness on the wettability performance of microstructured metallic surface using direct laser interference patterning. Materials 12(17):2737. https://doi.org/10.3390/ma12172737

45. Fadeeva E, Schlie-Wolter S, Chichkov BN et al (2016) Structuring of biomaterial surfaces with ultrashort pulsed laser radiation. In: Vilar R (eds) Laser surface modification of biomaterials: techniques and applications, pp 145–172. https://doi.org/10.1016/B978-0-08-100883-6.00005-8

46. Kim Y, Meade SM, Chen K et al (2018) Nano-architectural approaches for improved intracortical interface technologies. Front Neurosci 12:456. https://doi.org/10.3389/fnins.2018.00456

47. Buzea C, Pacheco II, Robbie K (2007) Nanomaterials and nanoparticles: sources and toxicity. Biointerphases 2(4):R17–R71. https://doi.org/10.1116/1.2815690

48. ISO/TR 10993-22 (2017) Biological evaluation of medical devices Part 22: guidance on nanomaterials

49. Chapman CAR, Chen H, Stamou M et al (2015) Nanoporous gold as a neural interface coating: effects of topography, surface chemistry, and feature size. ACS Appl Mater Interfaces 7(13):7093–7100. https://doi.org/10.1021/acsami.5b00410